Novel applications of the Monte Carlo method in polarization-sensitive optical coherence tomography approach

C. YU. ZENKOVA[1,*], O. V. ANGELSKY[1,2], D. I. IVANSKYI[1], P. A. RYABYI[1], YU. URSULIAK[3]
[1]*Research Institute of Zhejiang University-Taizhou, China*
[2]*Chernivtsi National University, Chernivtsi, Ukraine*
[3]*Municipal Enterprise Chernivtsi Regional Clinical Cardiological Center, Chernivtsi, Ukraine*

This study introduces novel solutions for reconstructing the structure of transparent biological media within the framework of polarization-sensitive optical coherence tomography. Reconstruction of the geometric phase, based on a modified Mach-Zehnder interferometer, enables mapping of the polarization architecture of the object, specifically the orientation of collagen fibers throughout the longitudinal scan. By accounting for scattering centers both in the epithelium and keratocytes in the cornea stroma, the depolarization of the object signal can be evaluated, which increases the signal-to-noise ratio toward the useful signal by four times. The impact of scattering on the object signal was assessed through mathematical modeling within the Monte Carlo approximation.

(Received January 13, 2025; accepted June 4, 2025)

Keywords: Monte-Carlo approach, Geometric phase, Mach-Zehnder interferometer, Signal depolarization, Scattering centers

1. Introduction

Optical Coherence Tomography (OCT) is a non-invasive imaging technique that provides high-resolution cross-sectional and longitudinal (lateral) images of tissue structures [1,2]. It is particularly valuable for examining organs where conventional diagnostic methods, like biopsy, are impractical. Widely used for detecting eye pathologies, OCT employs short femtosecond light pulses for optical ranging, analogous to how ultrasound uses sound waves, enabling detailed visualization of biological tissues. This technology bridges the gap between ultrasound imaging and microscopy [3].

OCT enables real-time acquisition of high-resolution three-dimensional images [4,5], made possible through rapid scanning speeds and efficient signal processing. The exceptional resolution allows for precise visualization of tissue architecture and morphology.

The technique operates using a two-beam interferometer paired with a broadband light source [1-5]. The optical path length varies in the sample arm of the interferometer, and interference fringes form only when the path lengths in the sample and reference arms match within the coherence length of the light source, typically between 2 and 15 μm. The coherence length determines the axial resolution, while the angular properties of the light source dictate lateral resolution.

Various advanced OCT techniques have emerged to enhance the study of biological tissues, including methods for reconstructing amplitude and phase information from biological samples. These advancements enable high-resolution tomographic imaging of blood flow, the generation of velocity maps, and precise localization of fluid dynamics for diagnostic purposes [6].

While OCT provides sufficient axial resolution for visualizing tissue structures, it has a notable limitation: it struggles to accurately assess individual thin nanolayers when they are damaged or disrupted. Addressing this challenge requires additional measurements beyond signal intensity. This is where Polarization-Sensitive OCT (PS-OCT) offers a solution, enhancing image contrast and providing more detailed insights into the sample being analyzed [7-10]. Recently we have introduced a non-invasive PS-OCT approach based on the modified Mach-Zehnder interferometer to reproduce geometric phase of a birefringent layer structure [11-13].

The geometric phase in this situation contains critical information about the polarization properties of the layer, specifically the orientation of the optical axis along the length of the longitudinal scan. This information enables precise identification of damaged regions within the object.

As light enters a biological object, such as the cornea of the eye, it interacts with the tissue's microstructure through multiple scattering events. These occur within specialized fibroblasts in the cornea stroma and as reflections from the surfaces of lamellae, driven by variations in the refractive index that define the tissue's architecture. The resulting object wave encodes critical information about the medium's properties, such as an amplitude information, light depolarization, phase shift, orientation of collagen fibers.

In this study, we propose a novel PS-OCT solution that combines a modified Mach-Zehnder interferometer with geometric phase approaches and the Monte Carlo method.

This integrated approach allows for detailed, high-quality structural analysis of biological samples. It enhances reconstruction accuracy for transparent and translucent objects by mitigating the effects of depolarization, improving the signal-to-noise ratio, and enabling deeper insights into the structural organization of biological object.

2. Scattering of photon packets in the framework of Monte Carlo approach

The cornea of the eye, as an optically transparent medium, consists of a set of layers (Fig. 1), each of which has a specific purpose in supporting visual function and forming the image on the retina.

In the first approximation, when forming the optical flow interacting with the stroma, we will disregard the absorption of the photon packet by the structure of the cornea. Instead, the focus will be on the mechanism of depolarization of the radiation during the scattering of the photon packet within the epithelium (the layer immediately following the precorneal tear film, Fig. 1) and the keratocytes, which serve as the scattering centers of the stroma.

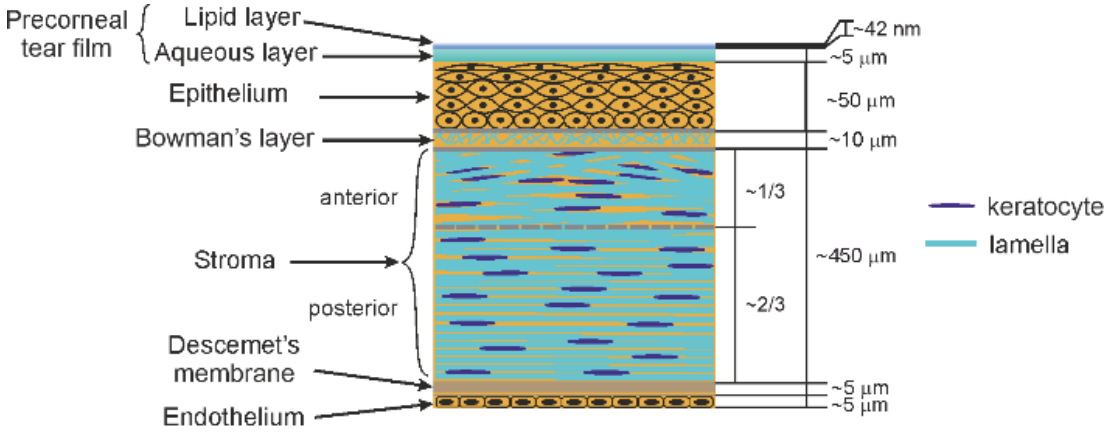

Fig. 1. Structure of eye cornea (colour online)

The nuclei of epithelial cells act as Mie scatterers, spherical in shape, with diameters ranging from 5 to 7 μm [14, 15]. The cytoplasm of the epithelium is characterized by a refractive index of $n_{cyt} = 1.36$, and the relative refractive index between the nucleus and cytoplasm is $m \equiv n_{nuc}/n_{cyt} = 1.06$ [15]. In the literature, for biological objects classified as soft particles ($m - 1 \ll 1$) with a size parameter $\xi = ka \gg 1$ (a being the radius of the nucleus), the Van de Hulst approximation theory [16] is commonly applied. This approximation effectively describes the scattering of light by these particles. The Van de Hulst approximation is a scalar scattering theory and can be employed for particles of arbitrary shape, not limited to spherical ones [16].

In the van de Hulst approximation, the effective scattering cross-section σ_s of the epithelial cell nucleus is defined as [14]:

$$\sigma_s = 2\pi a^2 \left[1 - \frac{\sin(2\chi(m-1))}{\chi(m-1)} + \left(\frac{\sin(\chi(m-1))}{\chi(m-1)}\right)^2\right], \quad (1)$$

$\chi = \xi n_{cyt}$ – the size parameter of the nucleus.

Then the scattering coefficient μ_s [17]: $\mu_s = \rho_N \sigma_s$, where ρ_N is a number density of particles. Then, according to preliminary estimates $\sigma_s = 74{,}56\ \mu m^2$, $\mu_s = 0{,}033\ \mu m^{-1}$.

The parameters of keratocytes involved in the modeling [18]: transverse length a = 30.9 ± 8.2 μm; thickness h = 1.34 ± 0.46 μm, depending on the thickness of adjacent lamellae. The area of the keratocyte cell body viewed in coronal (frontal) section was 292 ± 118 μm^2, which determines the longitudinal length b (Fig. 2). The nucleus occupies about 75% of the cell in the cross section and about 30-40% in the frontal section and is 1.02 ± 0.42 μm in thickness and 18.2 ± 6.0 μm in length.

The simulated keratocyte according to the entered geometric parameters is shown in Fig. 2.

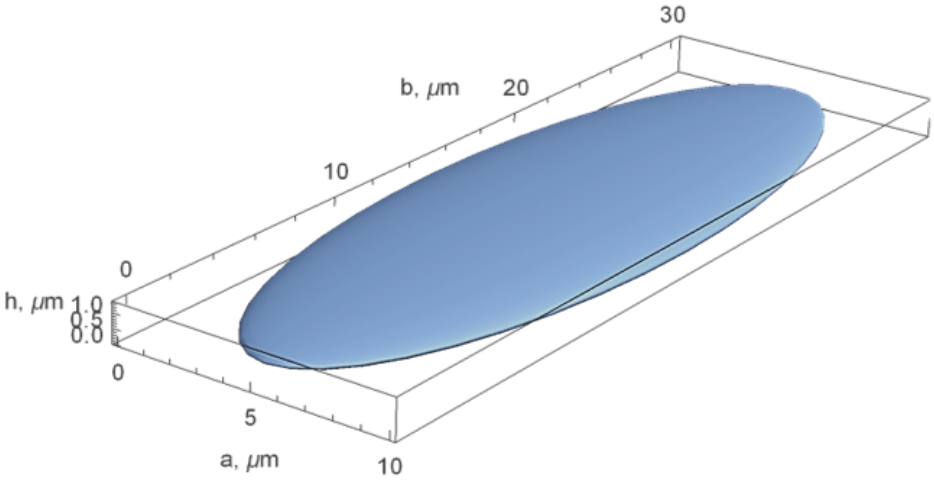

Fig. 2. Geometric model of keratocyte (a = 30 μm, b = 10 μm, h = 1.34 μm) (colour online)

The keratocyte is surrounded by extracellular fluid, the refractive index of which is $n_{base} = 1.356$ [17], the relative refractive index of the keratocyte is $m = n_{ker}/n_{base} = 1.018$. The particles are also optically soft. The size and value of the refractive index correspond to the Van de Hulst approximation [16]. The only difference is that keratocytes are not spherical particles, so the form of the scattering amplitude function will be different.

Another key aspect of the modeling is that, according to numerous experiments [19], keratocytes are the primary contributors to the back reflected optical flow. The amplitude reflection coefficient at the interface between the "extracellular fluid-keratocyte" is estimated as $r_{ker} = \frac{|n_{ker}-n_{base}|}{n_{ker}+n_{base}} = 0.00913$. Estimation of the weighting factor of the photon packet that is formed during reflection, $W_R \propto |\vec{E}_R|^2 \backsim 10^{-5}$ determines packet's contribution to the formation of the signal that comes out of the stroma, since it exceeds the value that determines the condition for the "disappearance" of photons (10^{-6}).

In the Van de Hulst approximation, the scattering amplitude function (according to (10), (11) $S_1(\theta,\varphi) = S_2(\theta,\varphi) = S(\theta,\varphi)$), for particles of arbitrary shape [16,17] can be written down $S(\theta,\varphi) = \frac{k^2}{2\pi}\iint(1 - \exp[-i\delta(\xi,\eta)])\exp[-ikr(\theta,\varphi)]\,dP$.

Integration is carried out over the entire plane of the geometric section of the particle P, the area of the geometric shadow (Fig. 3), which is formed in the plane $\vec{e}_\perp, \vec{e}_\parallel$, of the local coordinate system of the incident photon $(\vec{e}_\perp, \vec{e}_\parallel, \vec{u})$.

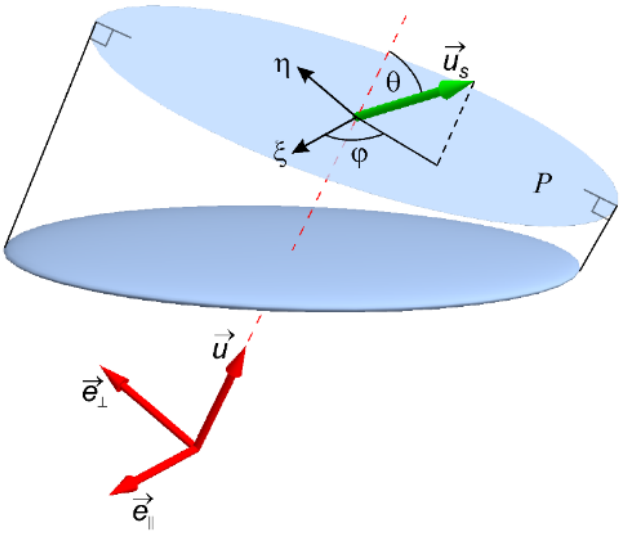

Fig. 3. Formation of the geometric shadow area P: $\vec{u}$ - directional vector of the incident photon, $\vec{u}_s$ - directional vector of the scattered photon, θ, φ - angles describing of scattering photon orientation $\vec{e}_\perp, \vec{e}_\parallel, \vec{u}$ - local coordinate system based on the incident photon, (ξ,η) – coordinates in the plane P (colour online)

Here $k = \frac{2\pi}{\lambda}$, where λ – wavelength in vacuum; $\delta(\xi,\eta) = kd(\xi,\eta)(m-1)$ – phase shift of a wave in a particle depending on the path length $d(\xi,\eta)$ of the beam in the particle's medium, (ξ,η) – are the points coordinates in the plane P, $\mathrm{r}(\theta,\varphi) = (\xi\cos\varphi + \eta\sin\varphi)\sin\theta$.

3. Monte Carlo approach for photon scattering in cornea

The interaction of photon packets with scattering centers is described in the approximation of the Monte Carlo approach [20]:

- *determination of the photon free path* [20] $l = -\frac{\ln\xi}{\mu_s}$ until the next act of interaction;

- *assessment of angles (Fig. 4) - the polar angle θ, which determines the scattering plane and the azimuthal angles φ (ψ) of rotation of the meridional planes*. Meridional planes are specified by the direction of the scattering vectors and their projection onto the XOY plane. The scattering plane is formed by the direction of the incident photon vector and the scattering vector for single scattering (Fig. 4, a) or the scattering vectors for multiple scattering (Fig. 4, b). Photon polarization is specified relative to the meridional planes of the initial photon and the scattered photon.

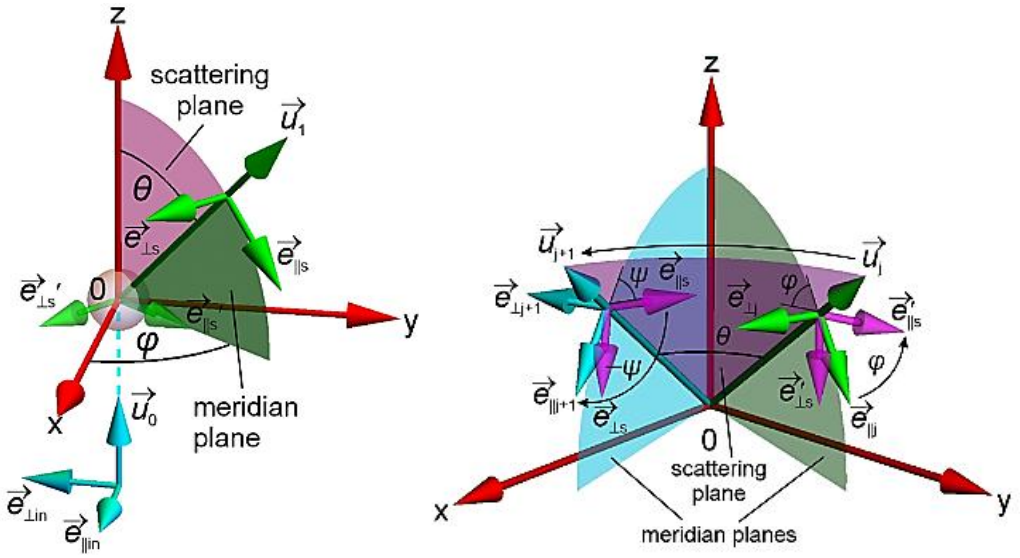

(a) *(b)*

Fig. 4. Determination of angles θ, φ, ψ for single (a) and multiple (b) scattering in the meridian planes Monte Carlo approximation [1]. Here $\vec{u}_0$ is the guiding vector of the incident photon, $\vec{u}_1$ is the guiding vector that determines the direction of the photon during single scattering (a), $\vec{u}_j$, $\vec{u}_{j+1}$ are the guiding vectors, respectively, for j (j+1) scattering events (b). Green (blue) planes are the introduced meridional planes, the position of which is specified by the angles φ, ψ, the purple one is the scattering plane, determined by the angle θ. $\vec{e}_\perp, \vec{e}_\parallel, \vec{u}$ – vectors defining a local orthonormal basis (colour online)

The initial weight of photon packets $W_i = T$, the number of packets 10^4, the initial direction of propagation, which sets the direction vector of the incident photon $\vec{u}_0 = (0,0,1)^T$, the initial polarization $\vec{\mathrm{E}}_0 = (-1,0)^T$, initial coordinates ($x_{rand}$, y_{rand}, z_0) of the photon position.

Condition: A section of 16 μm × 16 μm is selected, which is consistent with the cross section of the beam. As a first approximation, we will limit ourselves to the same weight of photon packets over the entire cross section, and take the wave front to be flat.

To determine angles in the meridian plane Monte Carlo approximation [21] it was introduced a local coordinate system with an orthonormal basis constructed from three vectors: the vector $\vec{u}$, which defines the direction of photon propagation, and the vectors $\vec{e}_\perp, \vec{e}_\parallel$, which define the components of the electric field perpendicular and parallel to the scattering plane, respectively. For a right-handed coordinate system, the following relationship holds [1]: $\vec{e}_\perp \times \vec{e}_\parallel = \vec{u}$.

If the guiding vector of the incident photon is $\vec{u}_0 = (0,0,1)^T$, then the parallel component $\vec{e}_{\parallel_{in}} = \vec{u}_0 \times \vec{e}_{\perp_{in}} = (1,0,0)^T$ [2], and the perpendicular component $\vec{e}_{\perp_{in}} = (0,-1,0)^T$, are directed opposite to the OY axis [21]. In this case, $\vec{e}_{\perp_{in}} \times \vec{e}_{\parallel_{in}} = \vec{u}_0$. The initial reference plane is the incident photon plane XOZ (Fig. 4a). The electric field of the incident beam can be represented in the local coordinate system $(\vec{e}_{\perp in}, \vec{e}_{\parallel in}, \vec{u}_0)$ as $\vec{\mathrm{E}}_{in} = E_{\parallel in}\vec{e}_{\parallel_{in}} + E_{\perp in}\vec{e}_{\perp_{in}}$, where $E_{\parallel in}$ $(E_{\perp in})$ are the parallel and perpendicular components, respectively.

Let the photon undergo a single scattering event (Fig. 4a). In this case, the coordinate system $(\vec{e}_{\perp in}, \vec{e}_{\parallel in}, \vec{u}_0)$ is transformed into a local coordinate system $(\vec{e}_{\perp_s}', \vec{e}_{\parallel_s}', \vec{u}_1)$, by rotating it by an angle φ, which is associated with the

direction of the photon after scattering $\vec{u}_1$ (Fig. 4a). The electric field vector is also transformed and is expressed as:

$$\begin{pmatrix} E'_{\parallel s} \\ E'_{\perp s} \end{pmatrix} = \begin{pmatrix} \cos\varphi & -\sin\varphi \\ \sin\varphi & \cos\varphi \end{pmatrix} \begin{pmatrix} E_{\parallel in} \\ E_{\perp in} \end{pmatrix}$$

$$\text{or } \vec{\mathrm{E}}'_s = R(\varphi)\vec{\mathrm{E}}_{in}, \tag{2}$$

$$\begin{pmatrix} E_{\parallel s} \\ E_{\perp s} \end{pmatrix} = \begin{pmatrix} S_2(\theta,\varphi) & S_3(\theta,\varphi) \\ S_4(\theta,\varphi) & S_1(\theta,\varphi) \end{pmatrix} \begin{pmatrix} \cos\varphi & -\sin\varphi \\ \sin\varphi & \cos\varphi \end{pmatrix} \begin{pmatrix} E_{\parallel in} \\ E_{\perp in} \end{pmatrix} \text{ or } \vec{\mathrm{E}}_s = S(\theta,\varphi)R(\varphi)\vec{\mathrm{E}}_{in}. \tag{3}$$

If the direction of propagation of the incident photon is arbitrary, i.e. in the case of multiple scattering, it is necessary to take into account the local orthonormal basis for each scattering vector, taking into account the rotation of the local coordinate system by angles φ, $-\psi$ respectively, and the formation of new local coordinate systems (Fig. 4b).

Then the resulting Jones vector for two arbitrary scattering events j and j+1 will be written as:

$$\begin{pmatrix} E_{\parallel s} \\ E_{\perp s} \end{pmatrix} = \begin{pmatrix} \cos\psi & \sin\psi \\ -\sin\psi & \cos\psi \end{pmatrix} \begin{pmatrix} S_2(\theta,\varphi) & S_3(\theta,\varphi) \\ S_4(\theta,\varphi) & S_1(\theta,\varphi) \end{pmatrix} \times \begin{pmatrix} \cos\varphi & -\sin\varphi \\ \sin\varphi & \cos\varphi \end{pmatrix} \begin{pmatrix} E_{\parallel in} \\ E_{\perp in} \end{pmatrix}. \tag{4}$$

If $S_1(\theta,\varphi) = S_2(\theta,\varphi) = S(\theta)$, $S_3(\theta,\varphi) = S_4(\theta,\varphi) = 0$, we can write

$$\vec{\mathrm{E}}_s = R(-\psi)S(\theta)\mathrm{R}(\varphi)\vec{\mathrm{E}}_{in}, \tag{5}$$

where $R(-\psi)$ matrix of rotation of the scattering plane to the subsequent position of the meridional plane associated with the subsequent orientation of the scattering vector.

In the case of multiple scattering, after the *K*-th event, the Jones vector is written as [22]:

$$\vec{\mathrm{E}}_K = \left[\prod_{j=1}^{K} R(-\psi_j)S(\theta_j)R(\varphi_j)\right]\vec{\mathrm{E}}_{in}. \tag{6}$$

It would like to note that all coordinate system transformations are described mathematically by rotation matrices and rotation transformations, which we used according to the proposed functions of the Mathematica software environment. The resulting amplitude and phase information after *K* scattering events, taking into account the free path length *l*, can be obtained by multiplying (7) by e^{iknl}:

$$\vec{\mathrm{E}}_K(l) = e^{iknl}\vec{\mathrm{E}}_K. \tag{7}$$

The resulting photon packet will continue to participate in subsequent interactions with scattering centers until it reaches the boundary between media and exits the layer. To estimate the angles (θ,φ) in the approximation of the polarized Monte Carlo model, the concept of a phase function [21] is used, which has the physical meaning of determining the probability density of photon scattering.

where $R(\varphi)$ – meridional plane rotation matrix (Fig. 4a).

Taking into account the scattering matrix $S(\theta,\varphi)$, which describes the processes associated with the scattering plane, the components of the electric vector relative to the scattering plane can be represented as:

For this model, the following form of the phase function [21] can be accepted:

$$P(\theta,\varphi) = s_{11}(\theta,\varphi) + s_{12}(\theta,\varphi)[Q_0\cos(2\varphi) + U_0\sin(2\varphi)]/I_0, \tag{8}$$

where $S_0 = [I_0, Q_0, U_0, V_0]^T$ – the Stokes vector of incident radiation, $s_{11}(\theta,\varphi)$ and $s_{12}(\theta,\varphi)$ – scattering matrix elements associated with amplitude scattering matrix elements $S_1(\theta,\varphi)$ и $S_2(\theta,\varphi)$ as follows [21]:

$$\begin{aligned} s_{11}(\theta,\varphi) &= \tfrac{1}{2}(|S_2(\theta,\varphi)|^2 + |S_1(\theta,\varphi)|^2) \\ s_{12}(\theta,\varphi) &= \tfrac{1}{2}(|S_2(\theta,\varphi)|^2 - |S_1(\theta,\varphi)|^2) \end{aligned}. \tag{9}$$

In the scalar case $S_1(\theta,\varphi) = S_2(\theta,\varphi) = S(\theta,\varphi)$, and determines the amplitude scattering function. Then $s_{11}(\theta,\varphi) = |S(\theta,\varphi)|^2$, $s_{12}(\theta,\varphi) = 0$. The phase function according to (8) will be written $P(\theta,\varphi) = s_{11}(\theta,\varphi) = |S(\theta,\varphi)|^2$. In the Van de Hulst scalar approximation, for spherical particles, the amplitude function becomes only a function of the scattering angle θ, i.e. $S(\theta,\varphi) = S(\theta)$ and can be written [16]:

$$S(\theta) = \chi^2 \frac{(1+\cos\theta)}{2}\frac{J_1(\chi\sin\theta)}{\chi\sin\theta}, \tag{10}$$

where J_1 – Bessel function (of 1st kind and 1st order).

If the phase function is only a function of the scattering angle θ then two uniformly distributed random variables are generated – $P_{rand} \in [0;1]$ and $\theta_{rand} \in [0;\pi]$. If $P_{rand}(\theta_{rand}) \le P(\theta_{rand})$, θ_{rand} is accepted as the scattering angle. Otherwise, the procedure is repeated. Deviation from the scalar approximation requires choosing a pair of angles: θ,φ. In the polarized Monte Carlo approach and the rejection method, the following conditions are applied to recover the phase function: three random variables are generated [21]: $0 \le \theta_{rand} \le \pi, 0 \le \varphi_{rand} \le 2\pi$ and $0 \le P_{rand} \le 1$. If $P_{rand} \le P(\theta_{rand},\varphi_{rand})$, then the angles $\theta_{rand},\varphi_{rand}$ are chosen.

Next, the direction of photons is evaluated after each scattering event, taking into account the resulting scattering angles θ,φ.

The histogram (Fig. 5) shows the probability distribution of N photons by scattering orders K. The "0th" order is the absence of scattering. According to the calculated parameters describing the scattering medium $\mu_s = 0{,}033\,\mu m^{-1}$, and using the total number of 5000

photons as an example, we can conclude that single scattering (N=1) dominates at 42.3%, 18.7% of photons do not scatter, and 39% of the photons undergo higher-order scattering events.

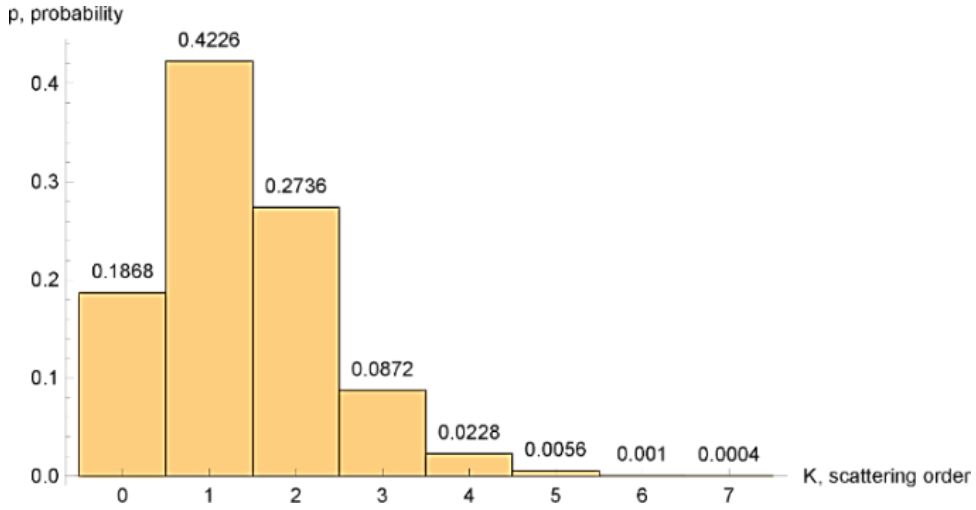

Fig. 5. Distribution of relative number of photons by scattering orders (colour online)

Scattering of photon packets on scattering centers determines depolarization of photon packets, which leads to the appearance of noise signals, a decrease in the level of the information signal.

Modeling the beam that contributes to forming the object signal, containing information about the structure of stromal lamellae and the distribution of keratocytes in the stroma, accounts for the depolarization of radiation due to scattering in the epithelium (Fig. 5). A preliminary estimate of the scattering coefficient of photon beams propagating through the keratocyte volume to a stromal depth of approximately 0.45 mm, considering the photon mean free path, indicates the dominance of single scattering. For single scattering, depolarization is virtually absent.

Therefore, we will assume that in the formation of the OCT signal, the influence of depolarization of photon packets due to scattering on keratocytes does not occur.

Modeling the scattering of a photon packet in the epithelium, using the meridian Monte Carlo method approximation, indicates with a 73% probability that photons interacting with the stroma will retain their polarization $\vec{E}_0 = (-1, 0)^T$ (Fig. 6a).

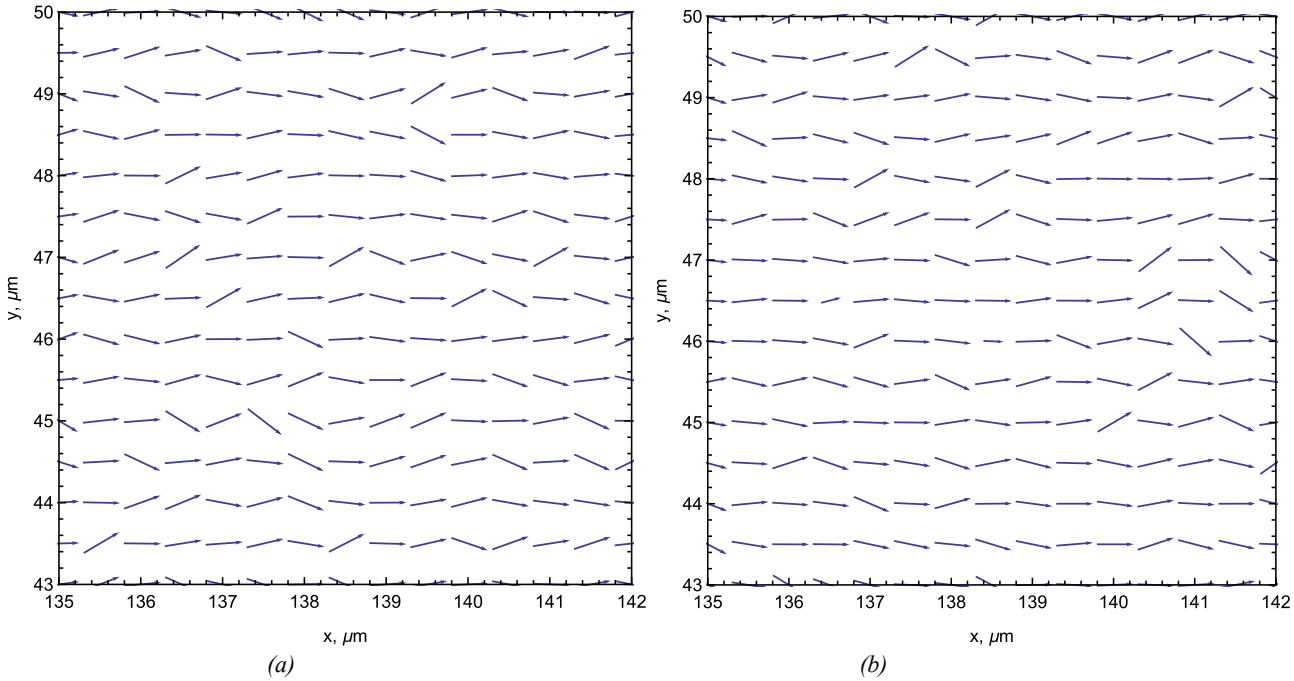

Fig. 6. Distribution of polarization in the transverse plane within the half-width of the beam when exiting the epithelium in the forward (a) and backward (b) directions (colour online)

The influence of the epithelium on beam polarization is also evident during reverse propagation, after interacting with the stroma (Fig. 6b). In this case, the degree of polarization reaches approximately 0.41 (Fig. 7, second red point). Depolarization was assessed using the relationship [23]: $P(d) \cong \frac{3}{2} e^{-d/l_p}$, where $l_p = 2.804 l_s$ is the characteristic length of depolarization for linear polarized wave, and $l_s = 1/\mu_s$ is the scattering mean free path.

The discrete distribution of photons allows to estimate the impact of depolarization on the level of the useful object signal during cornea scanning. Discrete points, where the signal is assessed, correspond to the pixels of the photosensitive matrix in the camera used [23]. This setup assumes either an averaging of depolarization within a pixel or the use of nanoaperture arrays with a 10 nm aperture diameter [23], facilitating nearly photon-by-photon scanning (Fig. 16). In this approach, an increase in the signal-to-noise ratio is observed, significantly enhancing the accuracy of lamella structure reconstruction and the localization of keratocytes.

This relationship is represented by the blue curve in Fig. 7. Additionally, depolarization was modeled using the Monte Carlo method, with the results approximated by a yellow curve that passes through the Monte Carlo-calculated data points (Fig. 7).

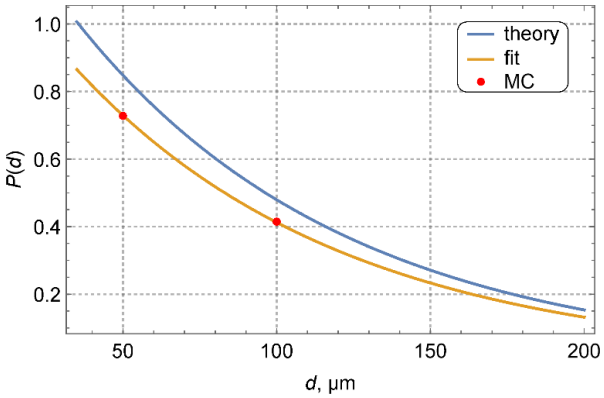

Fig. 7. Dependence of the degree of linear polarization on the length of the path of the linearly polarized beam $\vec{E}_0 = (-1, 0)^T$ through the epithelium. The red dots indicate the degree of polarization estimated in the forward direction (thickness of about 50 μm), backward (thickness of about 100 μm) using the Monte Carlo method. The blue curve is calculated theoretically, the yellow one is approximated by the obtained points (colour online)

After signal processing, a horizontally linearly polarized photon packet is directed onto each lamella. To form a linear polarization, we introduce into the probing beam a system that allows generating arbitrary polarization states, such as a QWP-HWP combination [24], a Berek compensator [25], or a polarization modulator (PM) (Fig. 14). With known depolarization parameters in the epithelium and the anisotropy of a specific lamella, the polarization of the probing beam is modeled to ensure that each lamella is illuminated by a horizontally linearly polarized beam. The frequency of the position change of the PM in XY directions, which determines its plane "polarization sensitivity", is significantly less than a fraction of a second, the frequency of regular jumps in eye movement.

To maintain this condition, a feedback loop connecting the central processor to the polarization modulator (PM) is essential. This feedback system compensates for the depolarization of the object signal and corrects deviations from the horizontally linear polarization state.

Proven methods of computer signal processing reduce the influence of the background signal caused by depolarization of radiation. As a result, the accuracy of stroma structure reproduction increases by 22.84%. The received object signal interacts with the reference beam.

4. PS-OCT signal formation

In the PS-OCT approach [26], a broadband light source such as a Ti:sapphire laser, with a spectral bandwidth of 170 nm and a central wavelength of 800 nm, achieves an axial resolution of $\delta z \approx 1.662$ μm in air. This resolution is well-suited for capturing the average thickness of lamellae. The axial resolution δz varies with the refractive index of the cornea, which changes with depth. For example, in the anterior stroma, where the refractive index is $n = 1.38$ [27], the axial resolution improves to 1.2μm, making it sufficient to resolve the stroma structure in detail.

Sample scanning is performed step-by-step, pixel-by-pixel, with the scanning resolution determined by the transverse resolution and depends on the numerical aperture (NA) of the beam [28]:

$$\delta x, y = \sqrt{2 \ln 2} \frac{\lambda_0}{\pi \cdot NA}. \quad (11)$$

The numerical aperture (NA) also determines the depth of focus ($b = \frac{n \cdot \lambda_0}{2\pi \cdot NA^2}$) of the beam in the medium [28]. Here n is the refractive index, λ_0 is the central wavelength. For compatibility with the sample thickness, which can reach up to 100 μm in the anterior stroma region, NA is set to 0.042. This configuration results in a depth of focus $b = 100$ μm and $\delta x, y = 7.15$ μm. The transverse resolution is sufficient to resolve the lateral dimensions of both the lamellae and keratocytes. Under these conditions, 28 × 28 transverse scans can be performed across a 200 μm × 200 μm area.

In the proposed model, the total interference signal generated by all photon packets within a single pixel is recorded, with the assumption that the depolarized component of the object field is minimized.

The interaction of the incident radiation with the cornea produces an object signal composed of N_d photon packets. These photon packets contribute to the formation of the OCT signal and are analyzed to reconstruct detailed information about the object under study.

Let the Jones vector of i-th photon packet at the exit from the medium is

$\vec{E}_i = \begin{pmatrix} E_{\parallel_i} \\ E_{\perp_i} \end{pmatrix} = \begin{pmatrix} A_{\parallel_i} e^{i\varphi_{\parallel_i}} \\ A_{\perp_i} e^{i\varphi_{\perp_i}} \end{pmatrix}$, where $A_{\parallel,\perp_i} = |\vec{E}_i|$ - amplitude components (horizontal (hor ($\parallel$) and vertical ($\perp$)) of the one photon packet of object signal, $\varphi_{\parallel,\perp_i} = \arg(\vec{E}_i)$ – phase components.

If photons do not interact with each other via interference, meaning the autocorrelation component is absent, the resulting intensity at the medium's output can be expressed as: $I = \sum_{i=1}^{N_d} A_{\parallel,\perp_i}^2$

To retrieve detailed information about the object under study, we employ the PS-OCT approach, as validated in previous studies [11–13]. This method utilizes a modified Mach-Zehnder interferometer (Fig. 8) and extracts information on both geometric and dynamic phases from the recorded interference signals. These signals are captured separately in the horizontal D1 and vertical D2 channels of the interferometer.

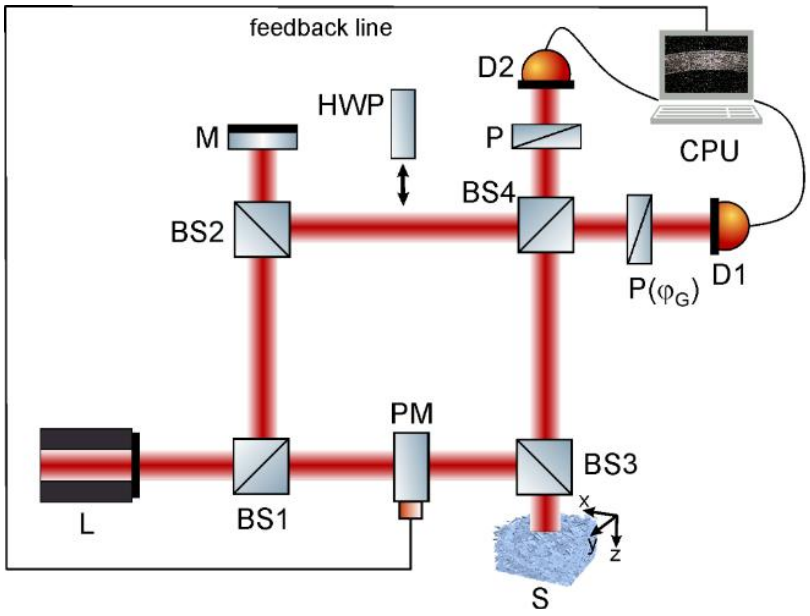

Fig. 8. The modified Mach-Zehnder interferometer scheme: L – radiation source; BS1, BS2, BS3, BS4 – nonpolarizing beamsplitters; M – reference mirror; z_r – optical path length in the reference arm, HWP – half-wave plate; D1, D2 – photodetectors; CPU – central processing unit; $P(\varphi_G)$ – polarizer in the horizontal channel allowing to restore the initial horizontal polarization of the beam, which makes it possible to estimate the geometric phase; P – polarizer in the vertical channel, allowing to recover the vertical component of the signal; PM – polarization modulator; S – sample. x, y, z – laboratory coordinate frame, connected with the beam propagation direction (colour online)

The formation of the OCT signal in this case occurs through the interaction of each individual photon packet with the reference wave. For modeling purposes, a section corresponding to the dimensions of one pixel, measuring 0.5 μm × 0.5 μm, is selected from the cross-section of the beam. Within this section, the signal is generated by eight photon packets. A detailed explanation of the approach for reconstructing geometric and dynamic phases using the interferometric method for a single lamella, characterized by a uniform volume distribution and disrupted collagen fiber orientation, can be found in our previous works [11–13].

The interference signals that are recorded in the horizontal and vertical channels can be written as:

$$I_{hor,ver}(z_r) = A_r^2 + \sum_{i=1}^{N_d} A_{\parallel,\perp_i}^2 + 2A_r \sum_{i=1}^{N_d} A_{\parallel,\perp_i} \cos(\varphi_{\parallel,\perp_i} - \varphi_0) \exp\left(-\left[\frac{2z_r - L_i}{l_c}\right]^2\right) \quad (12)$$

or:

$$I_{hor,ver}(z_r) = I_r + I_{\parallel,\perp} + 2A_r \sum_{i=1}^{N_d} A_{\parallel,\perp_i} \cos(\varphi_{\parallel,\perp_i} - \varphi_0)\, \Gamma(z_r).$$

Here A_r, $\varphi_0 = 2kz_r$ – amplitude module and phase of the reference wave correspondingly, z_r – optical path length in the reference arm, $\Gamma(z_r) = \exp\left(-\left[\frac{2z_r - L_i}{l_c}\right]^2\right)$ – coherence function, L_i – optical path length of the i-th photon packet in the medium, $l_c = \frac{2\ln 2}{\pi n}\frac{\lambda^2}{\Delta\lambda}$ – the coherence length in a medium with refractive index n determines the axial resolution $\delta z = l_c$ and defines the thickness of the optical material, i.e., the number of lamellae that can be resolved separately. In equation (16), the phase information

is contained in the high-frequency component $\cos(\varphi_{\parallel,\perp_i} - \varphi_0)$.

The incoherent superposition of the corresponding components determines the intensity background, which is eliminated by using additional polarizers.

The geometric phase is extracted by analyzing the phase distribution φ_{hor} of interferogram in the horizontal ($\parallel$) arm [11-13]:

$$\varphi_{hor} = \pi + \varphi_D + \varphi_G - \varphi_0. \quad (13)$$

Here $\varphi_D = 2\delta$ – a dynamic phase, $\varphi_G = \arctan(\tan\gamma\cos 2\alpha)$ – a geometric phase determined by the geometry of the birefringence media.

Information about the dynamic phase can be obtained by analyzing the interferogram from the vertical ($\perp$) arm, with a phase φ_{ver} between the superimposing components:

$$\varphi_{ver} = \frac{\pi}{2} + \varphi_D - \varphi_0. \quad (14)$$

According to (12)-(14) and results obtained in [11-13] the expressions for γ and α can be written:

$$\begin{cases} \gamma = \arccos\left[\pm\sqrt{\frac{A_\parallel^2}{1+\tan^2(\varphi_G)}}\right] \\ \alpha = \frac{1}{2}\arccos\left[\pm\tan(\varphi_G)\sqrt{\frac{A_\parallel^2}{A_\perp^2+\tan^2(\varphi_G)}}\right] \end{cases}, \quad (15)$$

where $A_\parallel = \sum_{i=1}^{N_d} A_{\parallel_i}$, $A_\perp = \sum_{i=1}^{N_d} A_{\perp_i}$ – obtained from envelopes magnitudes of the object signal in the horizontal and vertical channels of the interferometer.

Analysis of the obtained interference signals in two channels of the interferometer (Fig.9) ($I_{hor,ver}$) allows us to construct envelopes (A-scans) (Fig. 9 a, orange line) of the resulting signal ($A_{hor,ver}$) as [2, 29]: a complex analytical signal $\tilde{I}_{hor,ver} = A_{hor,ver}\exp(i\varphi_{hor,ver})$ is introduced, where $\varphi_{hor,ver} = \arg(\tilde{I}_{hor,ver}) = \mathrm{HT}[I_{hor,ver}]$ is an interferogram phase, obtained by the Hilbert transform (HT) of the interference distribution. $A_{hor,ver} = |\tilde{I}_{hor,ver}|$, which allows to extract information about the envelopes of the object signal $A_{\parallel,\perp}$ (Fig. 10, a, b). The resulting interferograms were obtained for the first and second surfaces of lamella.

The reflection coefficients at the object boundary are proportional to the amplitudes of the A-scans: $|r_{\parallel,\perp}| \sim A_{\mathrm{hor,ver}}^{max}$ and are related to the refractive indices of the media as $r_{\parallel,\perp} = f(n)$. The geometric thickness of the layers is determined as: $d = d_{opt}/n$.

Position of the envelope maxima in the horizontal channel $d_{1,2}$ allows us to find the geometrical path length (effective geometrical thickness of the lamella $d_{eff} = d_2 - d_1$) (Fig. 9a). The maximum of amplitudes distribution $A_{hor,ver}(d_2)$ for the second surface reproduce $A_{\parallel,\perp}$ (Fig. 9a, b). Phase of the interferogram (Fig. 10a,b) $\varphi_{hor2,ver2} = \varphi_{hor,ver}(z_2^{opt})$ give the value of the dynamic phase from the vertical channel: $\varphi_D = \varphi_{ver2} + \varphi_0 - \pi/2$ and the value of the geometric phase from the phase difference in the both channels: $\varphi_G = \varphi_{hor2} - \varphi_{ver2} + \pi/2$. z_1^{opt}, z_2^{opt} – the optical path lengths of the signal in the object arm.

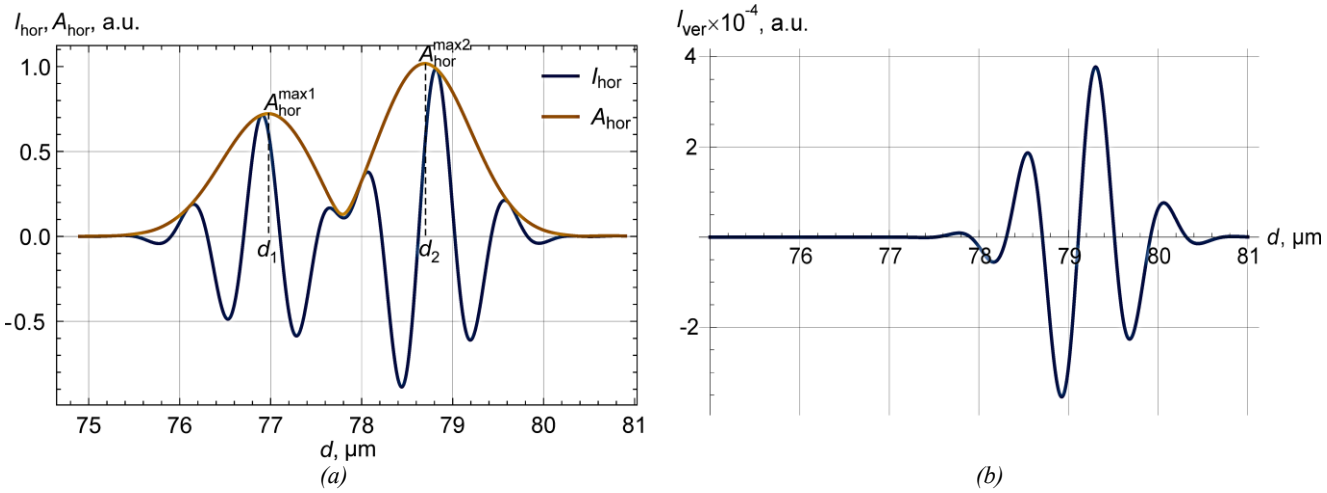

Fig. 9. The resulting interference (blue lines) signals in the horizontal (a) and vertical (b) channels of the interferometer, orange line indicates the distribution of modules of complex analytical signals for interferogram in the horizontal channel (colour online)

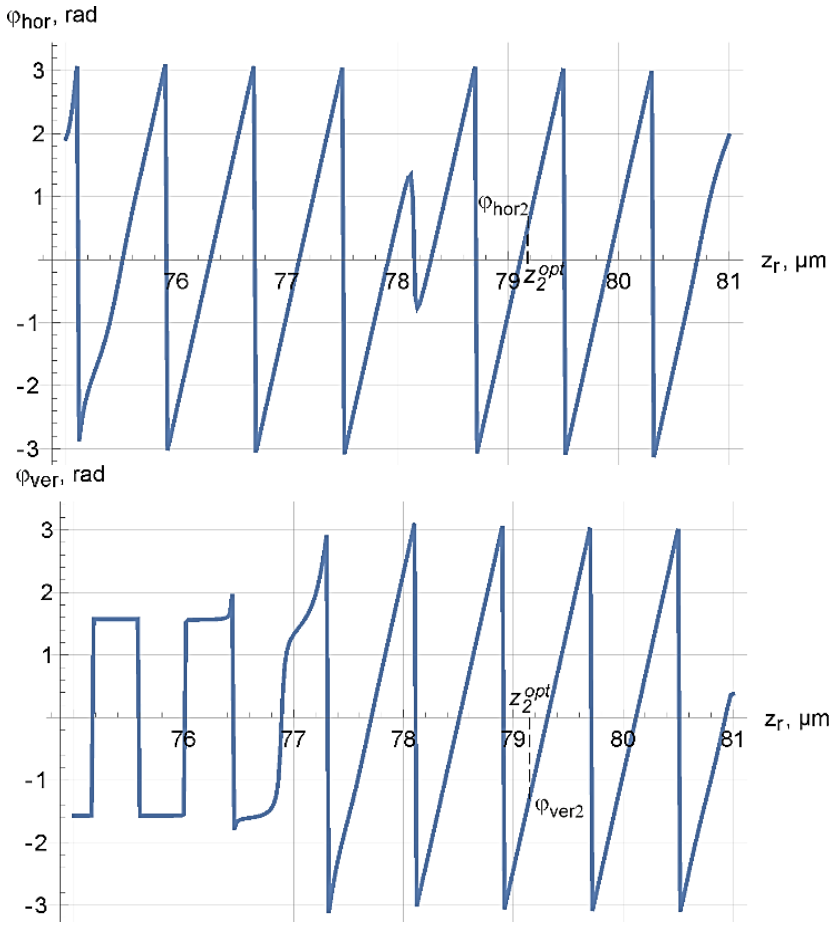

Fig. 10. Distribution phases (c-d) of complex analytical signals for interferograms in both channels of the interferometer. Here z_1^{opt}, z_2^{opt} – the optical path lengths of the signal in the object arm, which is formed by reflection from two surfaces of the lamella correspondingly, $\varphi_{hor2,ver2}$ – phases of the interferograms, which correspond to reflection from the inner surface of the lamella (colour online)

Birefringence of the lamella is also determined by the angle of deviation of the slow axis of the lamella β from the vertical direction ($\beta = 0$ when the slow axis is oriented along the axis z i $\beta = 90°$ when oriented in the horizontal plane). In the laboratory coordinate system $\Delta n(\beta) = n(\beta) - n_o$, where $n(\beta) = \frac{n_o n_e}{\sqrt{n_e^2 \cos^2\beta + n_o^2 \sin^2\beta}}$ [30]. If the refractive indices of the medium n_o, n_e are known or can be theoretically calculated, then the angle β can be found from the analysis of the simulated dependencies $n(\beta)$ or $\Delta n(\beta)$ for the known value of birefringence (refractive index) of the medium (Fig. 13).

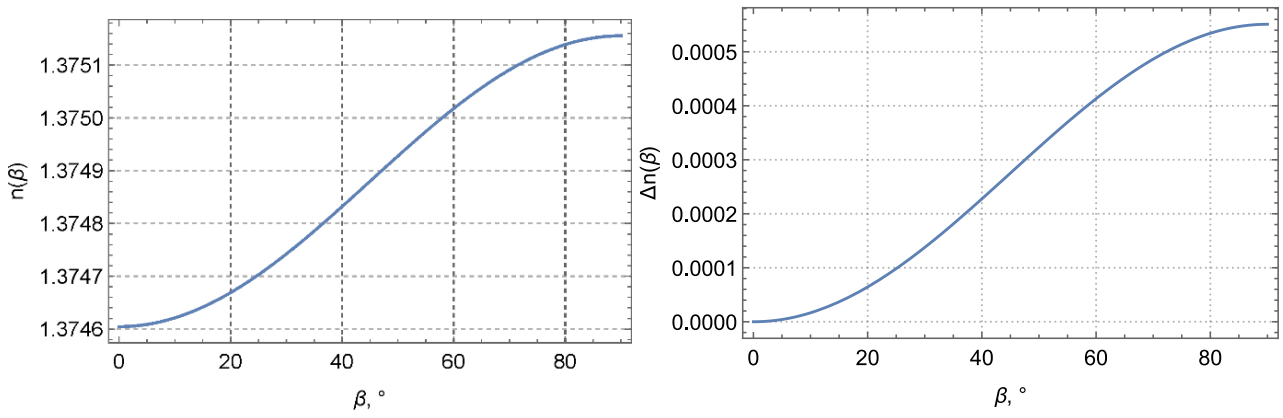

Fig. 13. Dependence of birefringence $\Delta n(\beta)$ and refractive index $n(\beta)$ on the angle of deviation of the slow axis of the lamella β (colour online)

The main results obtained from the above described analysis are the reflection coefficient from the first (upper) surface of the lamella $r_{1\parallel}$, the moduli of the amplitude components of the object field $A_{\parallel,\perp}$, the effective optical thickness d_{eff}^{opt} (or the dynamic phase φ_D) and the geometric phase φ_G. The following parameters of the lamella are obtained from the modeled values: the average refractive index $\bar{n} = 1.37248$, the effective thickness $d_{eff} = 1.4527$, the phase delay $\gamma = 0.00554$, the angle $\alpha = 52.55°$, the birefringence $\Delta n(\beta) = 5.1456 \times 10^{-4}$ and angle $\beta = 75.3°$. The errors of the obtained parameters are: $\varepsilon_\alpha = 1{,}86\%$, $\varepsilon_\beta = 1{,}46\%$, $\varepsilon_\gamma = 4.97\%$, $\varepsilon_{\bar{n}_l} = 0{,}173\%$, $\varepsilon_{\Delta n} = 0{,}86\%$, $\varepsilon_{deff} = 0.17\%$.

The results of the simulation are presented in the next figure (Fig. 14).

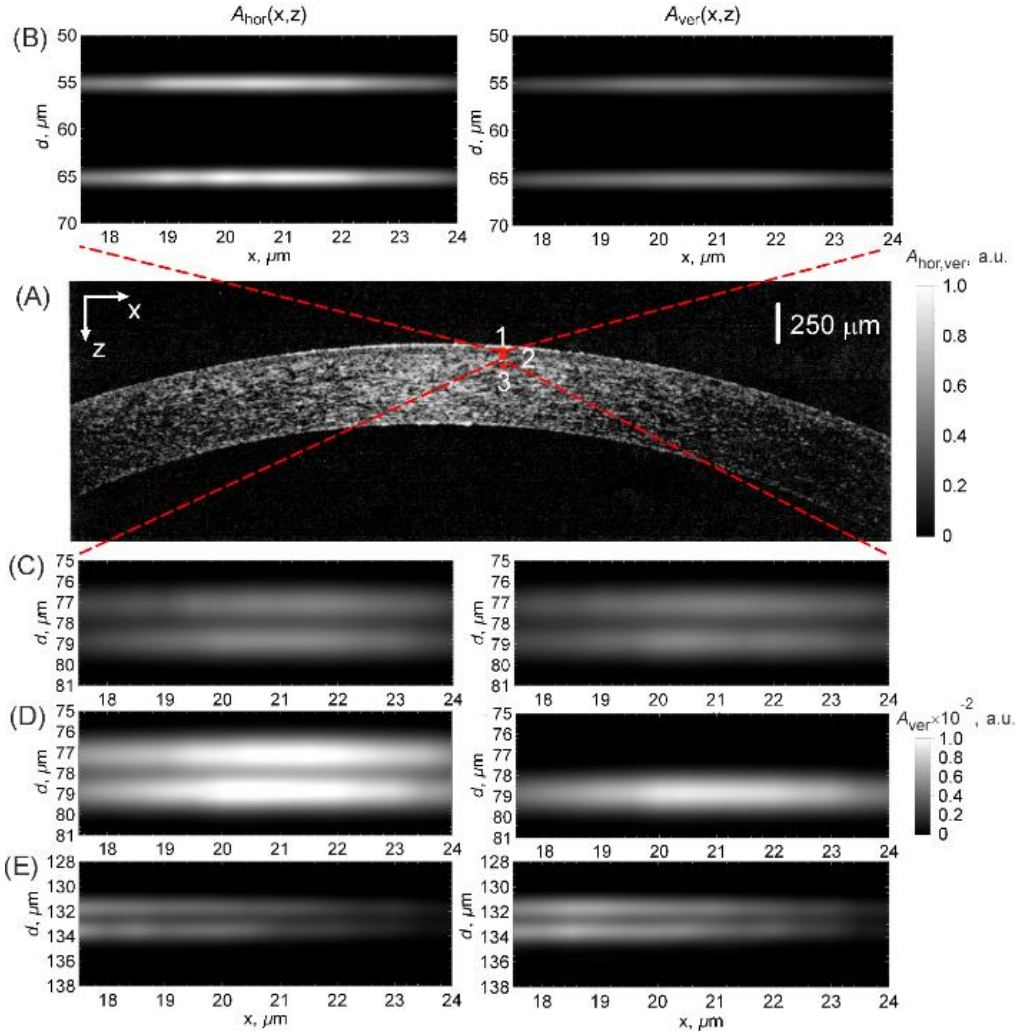

Fig. 14. Reconstructed structure of the cornea. Here (A) represents the OCT image of the cornea; (B), (C), (D), and (E) show two-dimensional signal distributions (B-scans) in horizontal $A_{hor}(x,z)$ (left column) and vertical $A_{ver}(x,z)$ (right column) channels of the interferometer for different regions of the cornea: 1- Bowman's layer (B); 2- lamella (C, D); 3 - keratocyte (E). Bright areas define the boundaries of separation (colour online)

The signal level is presented in a linear scale in relative units to the real geometric depth of the medium d (Fig. 14). The transverse dimensions of sections 1,2,3 correspond to the half-width of a Gaussian beam (~7 μm); the pixel dimensions are 0.5×0.5 μm^2. Each B-scan (Fig. 14(B)-(E)) contains 14 A-scans in the transverse direction x. The signal inside each pixel is generalized by the number of photons in it.

5. Conclusion

The given paper is a continuation of the cycle of works on polarization-sensitive optical coherence tomography, which presents a new approach to reconstructing the fine structure of biological anisotropic objects based on a modified Mach-Zehnder interferometer using a geometric phase.

To increase the signal-to-noise ratio of reconstructing the architecture of the cornea, it is proposed to take into account the signal depolarization, which is the result of scattering of radiation on the scattering centers of the cornea. The simulation of photon packet propagation in the cornea is performed using the meridian plane Monte Carlo approximation, within which the object and interference signals are simulated with the reproduction of the spatial architecture of the cornea structure. The introduced feedback loop, connecting the computer module with the polarization modulator, allows for control of the probing signal by forming a horizontally linearly polarized beam before each subsequent lamella during sample scanning within the depth of the scan in real time. Extraction of information about the geometric and dynamic phases allowed us to reconstruct the structure of birefringent lamellas, and evaluation of interference signals in both channels of the interferometer provided a complete picture of the localization of scattering centers in the eye cornea.

References

[1] W. Drexler, J. G. Fujimoto, Optical Coherence Tomography. Technology and Applications, Springer International Publishing, Switzerland, 2015.

[2] S. Ramamoorthy, Y. Zhang, T. Petrie, A. Fridberger, T. Ren, R. K. Wang, S. L. Jacques, A. L. Nuttal, Journal of Biomedical Optics **21**(2), 025003 (2016).

[3] A. Unterhuber, B. Pova ay, K. Bizheva, B. Hermann, H. Sattmann, A. Stingl, T. Le, M. Seefeld, R. Menzel, M. Preusser, H. Budka, C. Schubert, H. Reitsamer, P. K. Ahnelt, J. E. Morgan, A. Cowey, W. Drexler, Phys. Med. Biol. **49**(7), 1235 (2004).

[4] S. Zheng, Y. Bai, Z. Xu, P. Liu, G. Ni, Front. Phys. **9**, 744346 (2021).

[5] R. Bernarders, J.Cunha-Vaz, Optical Coherence Tomography, Biological and Medical Physics, Biomedical Engineering, Spinger-Verlag Berlin Heidelberg, 2012

[6] Z. Chen, T. E. Milner, X. Wang, S. Srinivas, J. S. Nelson, Photochem. Photobiol. **67**(1), 56 (1998).

[7] M. Pircher, K. Christoph, U. Hitzenberger, Sh. Erfurth, Progress in Retinal and Eye Research **30**(6), 431 (2011).

[8] F. de Boer Johannes, Th. E. Milner, Journal of Biomedical Optics **7**(3), 359 (2002).

[9] M. C. Pierce, M. Shishkov, B. H. Park, N. A. Nassif, B. E. Bouma, G. J. Tearney, J. F.de Boer, Opt. Express **13**, 5739 (2005)

[10] W. Drexler, Y. Chen, A. D. Aguirre, B. Považay, A. Unterhuber, J. G. Fujimoto, Ultrahigh Resolution Optical Coherence Tomography, Springer, Cham., 2015.

[11] O. V. Angelsky, A. Ya. Bekshaev, C. Yu. Zenkova, D. I. Ivanskyi, J. Zheng, M. M. Chumak, Frontiers in Physics **11**, 1260830 (2023).

[12] C. Yu. Zenkova, O. V. Angelsky, D. I. Ivanskyi, M. M. Chumak, Physics and Chemistry of Solid State **24**(4) 729 (2023).

[13] C. Yu. Zenkova, D. Ivanskyi, M. Diachenko, M. Chumak, Proc.SPIE **12938**, 129380A (2024).

[14] V. Turzhitsky, L. Qiu, I. Itzkan, A. A. Novikov, M. S. Kotelev, M. Getmanskiy, V. A. Vinokurov, A. V. Muradov, L.T. Perelman, Applied Spectroscopy **68**(2), 133 (2014).

[15] L. T. Perelman, V. Backman, M. Wallace, G. Zonios, R. Manoharan, A. Nusrat, S. Shields, M. Seiler, C. Lima, T. Hamano, I. Itzkan, J. Van Dam, J. M. Crawford, M. S. Feld, Physical Review Letters **80**(3), 627 (1998).

[16] H. C. van de Hulst, Light scattering by small particles, John Wiley and Sons, New York, Chapman and Hall, London, 470 (1957).

[17] Valery V. Tuchin, Tissue Optics: Light Scattering Methods and Instruments for Medical Diagnostics, Third Edition SPIE Press, 9781628415179 (2015).

[18] M. J. Doughty, W. Seabert, J. P. Bergmanson, Y. Blocker, Tissue and Cell **33**(4), 408 (2001).

[19] G. Xiong, P. Xue, J. Wu, Q. Miao, R. Wang, L. Ji, Opt. Express **13**, 2182 (2005).

[20] M. Schürmann, J. Scholze, P. Müller, J. Guck, C. J. Chan, Journal of Biophotonics **9**(10), 1068 (2016)

[21] J. M. Tiffany, Current Eye Research **5**(11), 887 (1986).

[22] V. Backman, R. Gurjar, K. Badizadegan, I. Itzkan, R. R. Dasari, L. T. Perelman, M. S. Feld, IEEE Journal of Selected Topics in Quantum Electronics **5**(4), 1019 (1999).

[23] J. Andrew, H. C. Gomes, M. B. Wolfsen, Wallace, K. C. Frances, V. Backman, Opt. Express **22**, 5325 (2014).

[24] D. Lopez-Mago, A. Canales-Benavides, R. I. Hernandez-Aranda, J. C. Gutiérrez-Vega, Optics Letters **42**(14), 2667 (2017).

[25] N. Lippok, S. Coen, R. Leonhardt, P. Nielsen, F. Vanholsbeeck, Opt. Lett. **37**(15), 3102 (2012).

[26] A. J. Radosevich, J. D. Rogers, I. R. Capoğlu, N. N. Mutyal, P. Pradhan, V. Backman, Journal of Biomedical Optics **17**(11), 115001 (2012).

[27] V. Wang, S. L. Jacques, L. Zheng, Comput. Methods Programs Biomed. **47**, 131 (1995).

[28] G. F. Bohren, D. R. Huffman, Absorption and Scattering of Light by Small Particles, New York, Wiley, 1998.

[29] S. Hannes, A. D. V. Santos, D. Schmidl, G. Garhöfer, A. Fard, H. Bagherinia, L. Schmetterer, R. M. Werkmeister, Cornea **42**(4), 490 (2023).

[30] F. Jaillon, H. Saint-Jalmes, Applied Optics **42**(16), 3290 (2003).

*Corresponding author: k.zenkova@chnu.edu.ua